Modelling the complex evaporated gas flow and its impact on particle spattering during laser powder bed fusion

Jürgen Jakumeit[a], Gongyuan Zheng[a], Romuald Laqua[a], Samuel J. Clark[b,c*], Jonas Zielinski[d], Johannes H. Schleifenbaum[d], Peter D. Lee[b]

[a]Access e.V., Intzestr. 5, 52072 Aachen, Germany
e-mail: jakumeit@access-technology.de, web page: http://www.access-technology.de
(corresponding author: Jürgen Jakumeit)

[b]Department of Mechanical Engineering, University College London, WC1E 7JE, UK
email: peter.lee@ucl.ac.uk

[c] X-ray Science Division, Argonne National Laboratory, Lemont, IL 60439 email: sjclark@anl.gov

[d] RWTH Aachen University – chair for Digital Additive Production (DAP)
Campus Boulevard 73, 52074 Aachen, Germany
e-mail: Jonas.Zielinski@DAP.Rwth-Aachen.de- Web page: http:// www.dap.rwth-aachen.de

[*]Current address: X-ray Science Division, Argonne National Laboratory, 9700 S Cass Ave, Lemont Il USA.

ABSTRACT

The additive manufacturing (AM) of metals is becoming an increasingly important production process with the potential to replace traditional techniques such as casting. Laser Powder Bed Fusion (LPBF) is used in many applications to print metal parts from powder. The metal powder is heated locally with sufficient laser radiation that the liquid melt easily reaches its boiling temperature, which leads to a metallic vapour jet that can entrain both powder bed particles and molten droplets. The small size of laser-matter interaction site makes a detailed experimental analysis of the process challenging. Synchrotron X-ray imaging experiments are one of the few methods which can capture the dynamic melting and solidification processes. Comparing such experiments with computer simulations of the process is an important approach in order to better understand the manufacturing process and to analyse the influence of process parameters on the *evaporated gas jet and the acceleration of individual particles, which can easily lead to a deteriorated AM component quality*.

The melting and solidification of the metal powder is simulated using an Eulerian multiphase approach based on a control volume discretization of powder bed and substrate and a volume of liquid separation from melt and gas phase. The gas phase modelled as an ideal gas reaches velocities up to 100 m/s. Lagrangian particle tracking in the simulation demonstrates that the velocity fields calculated by the Eulerian multi-phase approach in combination with a standard drag-force model lead to particle accelerations in good agreement with those measured experimentally. In order to avoid numerical laborious Lagrangian calculations, a direct method to compare an Eulerian multiphase simulation with synchrotron X-ray experiments was introduced and validated. This approach is used to analyse the influence of process parameters including laser power and laser speed *on the acceleration of particles from the melt pool area*. While the particle acceleration increases linearly with line energy in the conduction mode, a linear decrease

of the acceleration with increasing line energy can be found in the transition mode before the acceleration increases again with line energy in the keyhole mode.

1. INTRODUCTION

Additive Manufacturing (AM) promises the aerospace, automotive and biotechnology sectors, among others, unprecedented freedom in the design phase in comparison to traditional manufacturing techniques. The geometrical freedom and integration of optimization strategies into the design process makes AM very attractive for increased performance and personalized production [1, 2].

Laser Powder Bed Fusion (LPBF) is used in many applications for printing metal parts from powder [3, 4]. The powder is added layer by layer and heated locally by a laser beam, a small area of the new powder layer being melted. [5]. Metal powder made from alloys based on iron [3], nickel [4], titanium [5, 6] and aluminium [7] were processed by LPBF. Large scale use of metal AM is still hampered by the poor reliability and predictability of the properties of the components. Our understanding of the influence of powder properties, process parameters and equipment on part quality must be improved in order to enable precise control of the process and to achieve reliable part quality [8, 9].

Recently, much attention has been paid to the defect generation by spattered particles, which may change the powder composition or layer height if they fall on unprocessed regions or increase the surface roughness at already processed regions. It has been observed that particles move into the melt pool from the surrounding region and can be accelerated out of the melt pool before melting by the high-speed gas stream [9]. Radiographs of the melt pool dynamics reveal that a significant number of particles are accelerated out of the melt pool and scattered onto both processed and unprocessed regions. An understanding and control of this process is required to achieve a stable building process.

In addition to synchrotron X-ray imaging, computer simulations can be an important tool to understand particle spraying. A meaningful modelling of spattering during melting and solidification in LPBF processes requires the resolution of the phenomena down to the powder particle scale. In the meantime, various simulation frameworks have been developed by various groups in recent years to model LPBF and related processes based on a continuum mechanical approach [10–17]. A comprehensive review of simulation of melt pool behaviour during AM is given by Cook et al. [18]. The process simulations often use a realistic powder particle distribution calculated by the discrete-element method (DEM) placed on a solid substrate. Heating of the powder bed by the laser light can be modelled using a ray tracing algorithm [19] for a realistic description of the light absorption, a simpler laser light radiation from the top or an energy deposition described by a depth dependent profile [20], which is calibrated by comparison to experiments [21]. Cooling of the melt includes energy loss due to light radiation and heat conduction through powder and substrate. The evaporation of the metal is taken into account through a heat loss due to evaporation and the change of the melt front by the recoil pressure. The approaches mentioned so far calculate temperature change and flow only in the melt but not in the gas. A correct handling of the gas phase as an ideal gas was added by Panwisawas *et al.* [22] to analyse the conditions for keyhole formation and porosity in laser fusion welding [23]. The group of Körner et al. developed a simulation of electron- and laser-PBF processes based on the Lattice-Boltzmann method [24, 25]. Simulation of metal evaporation was added to this approach [26] without modelling velocity and temperature distribution in the gas phase as well as a calculation of the developing microstructure by a cellular automaton [27]. Recently, the dynamics of the gas phase during metal evaporation and particle spattering was investigated by numerical modelling and comparison to experiments for a simplified welding setup [28], a stationary LPBF process [29] and LPBF-processes described by gas phase and metal vapour jet coupled to a discrete element model to calculate particle trajectories [30].

Here, metal powder melting and solidification is simulated using an Eulerian multiphase approach based on a control volume discretization of powder bed and substrate and a volume of liquid separation from melt and gas phase provided by the computational-fluid-dynamics (CFD) solver STAR-CCM+ (version 2020.2, see also [31]). The methodology includes models for metal powder heating by the laser beam and metal evaporation. Trajectories of spattering particles are calculated using a simple Lagrangian calculation of the single particle acceleration in the gas (see theory section 2). A comparison of calculated melt pool depth and width with experimental observations is presented to validate the Eulerian simulation approach (section 3). A comparison of particle trajectories calculated by the Lagrangian model and an averaging analysis to the trajectories from synchrotron X-ray images demonstrates the correct description of the phenomena controlling spattering events (section 4): the combination of Eulerian multiphase approach to determine the gas velocities and Lagrangian calculation to derive the particle acceleration describes the particle scattering phenomena correctly. Based on this combined model a new volume averaging methodology was developed to calculate the acceleration of single particles based on the Eulerian model without computational expensive Lagrangian calculations (section 5). Fig. 1 shows a flow chart of the newly developed modelling approach. Using this methodology the influence of AM process parameters on the keyhole shape, gas velocity dynamics and particle acceleration for In718 and Ti6Al4V single-track experiments is analysed. A summary and outlook conclude this work.
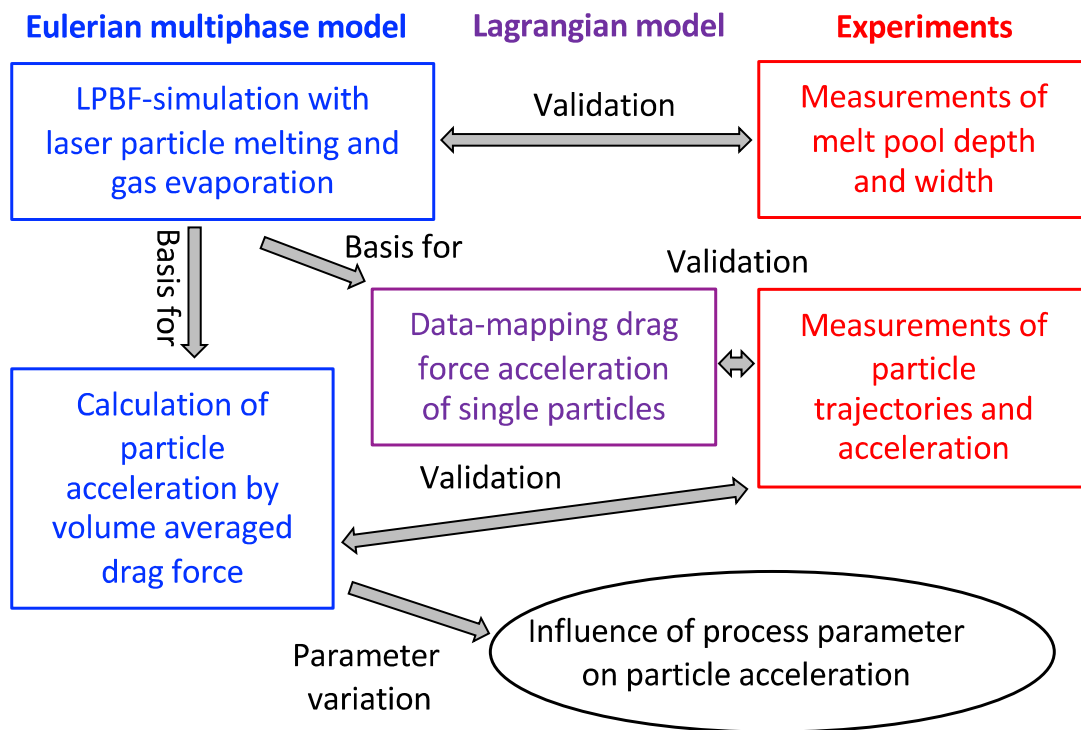

Fig. 1: Flow chart of the modelling approach

2. SIMULATION APPROACH

The co-existing gas, melt and solid phases in the LPBF-process can be described via a continuum mechanics approach. The equations describing mass, momentum and energy are given by [32]:

$$\frac{\partial}{\partial t}\int_V \rho\,dV + \oint_S \rho\boldsymbol{v}\,ds = 0 \tag{1}$$

$$\frac{\partial}{\partial t}\int_V \rho\boldsymbol{v}\,dV + \oint_S \rho\boldsymbol{v}\boldsymbol{v}\,ds = \oint_S \boldsymbol{T_C}\,ds + \int_V (\rho\,\boldsymbol{F_b} + S_s + S_d)\,dV \tag{2}$$

$$\frac{\partial}{\partial t}\int_V \rho h\,dV + \oint_S \rho h\boldsymbol{v}\,ds = \oint_S \boldsymbol{q}\,ds + \int_V S_h\,dV \tag{3}$$

$$\frac{\partial}{\partial t}\int_V f_m\,dV + \oint_S f_m\,\boldsymbol{v}\,ds = 0 \tag{4}$$

where t the time, $\boldsymbol{v}$ is the velocity vector, $\boldsymbol{T_C}$ is the Cauchy stress tensor, $\boldsymbol{q}$ is the heat flux vector, ρ the density, $\boldsymbol{F_b}$ is the body force, h is the thermal enthalpy and V the volume of a cell bounded by the surface S. Several physical phenomena are coupled to the set of equations by source terms. The enthalpy source term S_h describes the release of latent heat of melting L_{melt} proportional to the change in fraction of solidified melt given by tabulated fraction solid (fs) values as function of temperature T: $S_h = L_{melt}*d(fs(T))/dT$ [33]. A volume of fluid (VoF) method with a volume fraction of melt function f_m describes the melt/gas interface. A high-resolution interface capturing (HRIC) scheme ensures a sharp interface throughout the simulation [33]. The melt is treated as a compressible liquid with a temperature-dependent viscosity. For fs values greater than 0.3, the flow resistance of the dendrite network of the solidifying melt S_d is calculated using Darcy's law and an estimate of the permeability of the dendrite network using the Kozeny-Carman equation [31]. Gas is treated as ideal gas with a temperature dependent viscosity ($\mu(T) = \mu_{ref} * (T/T_{ref})^\alpha$). The temperature-dependent viscosity and flow resistance of the dendrite network are insufficient to prevent slow deformation of cold powder particles due to the creep of the solid metal. The flow resistance and the viscous resistance depend on the flow velocity and are small for low velocities. The cold melt therefore shows creep behaviour if only the two resistances hinder the movement of the melt. In order to model a realistic solid cold metal, a flow-stop model was implemented, which sets the velocity to zero and prevents further solving of the momentum equation (2) if the solids content of the melt is above a critical value.

The surface tension source term S_s is modelled using a continuum surface force model [34]. The normal $S_{s,n}$ and tangential component $S_{s,t}$ of the surface force are calculated by:

$$S_{s,n} = -\sigma\nabla\left(\frac{\nabla f_m}{|\nabla f_m|}\right)\nabla f_m, \qquad S_{s,t} = (\nabla\sigma)_t|\nabla f_m|, \tag{5}$$

where σ is the surface tension coefficient, $(\nabla\sigma)_t$ is the gradient of the surface tension coefficient in the tangential direction. Where $(\nabla\sigma)t$ is temperature dependent and, therefore, varies along the surface of the melt pool due to temperature differences, the tangential part does not vanish. In this case, Marangoni or Bénard convection can develop tangential to the free surface.

The laser heating of the powder bed is an important aspect of LPBF processes. During the process the laser power and spatial distribution of intensity can be monitored, while the amount of heat absorbed by the powder is difficult to measure and depends on the depth and shape of the keyhole. Allen et al. [21] recently presented an analysis of this problem by simultaneously measuring the keyhole depth and absorption of the laser light and thereby uncovering different absorption behaviour during conduction, transition and keyhole regime. In the area of process simulation, various approaches are reported to model the heating of the powder by the laser, which can be sorted into three main groups with increasing complexity: energy deposition described by a profile [20], vertical radiation of the powder without reflection and full ray tracing algorithms [10, 12].

A two-step approach is used here, which can be sorted into the second group of vertical radiation. First, the surface irradiated by the laser is marked with a participating media radiation model. A light beam that is limited to four times the standard deviation (σ) of the Gaussian laser profile irradiates the powder from the top of the simulation domain, and metal surfaces are marked for energy deposition when the absorbed heat of the light beam exceeds a threshold value. Fig. 2a,b show the marked region for the IN718 application with shallow keyhole and the Ti6Al4V application with deep keyhole. Second, the marked metal surfaces are heated by a volumetric heat source VHS_{laser} with a radial dependence of the energy flux to model the heating of a laser with a given beam profile (Gaussian throughout this work). Fig. 2c,d show the Gaussian distribution of the amount of deposit energy for the IN718 c) and Ti6Al4V d) application.

The participating media radiation-based approach leads to a thicker energy deposition area at the bottom of the deep keyhole (Fig. 2 b) compared to the shallow keyhole (Fig. 2a). Fig. 2f shows that the VoF-surface is not sharp in case of the deep keyhole as in case of the shallow keyhole (Fig. 2e) due to the highly dynamic melt pool behaviour at higher laser power (see simulation results in section 4+5). The ragged metal surface leads to a deeper penetration of the laser beam and,
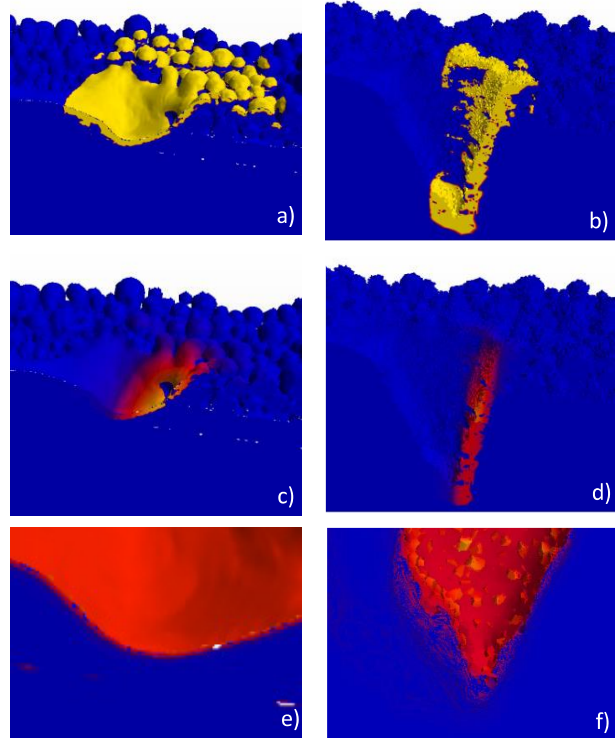

Fig. 2: Marked region for laser energy deposition (a+b), power entered by the VHS (c+d) and VoF surface (e+f) for a shallow keyhole in IN718 (a,c,e) and a deep keyhole in Ti6Al4V (b,d,f).

consequently, to a thicker region of energy deposition. These results show that the participating media radiation-based approach is able to capture effects in connection with melt pool dynamics. A quantitative validation is difficult and not the topic of this work. In addition, the new approach to model laser irradiation is able to handle light reflection by the metal surfaces and light absorption by evaporated metal; both effects are planned as future developments.

The calculation of VHS_{laser} from the power of the source of the participating media radiation is complex. Therefore, VHS_{laser} was used as simulation parameter. For a comparison to measurements the laser power (P_{laser}) can be calculated from VHS_{laser} by an absorption coefficient, which can depend on P_{laser}, VHS_{laser} or the keyhole shape. In this way, a calibration of radiation model parameter like absorptivity and reflectivity of the metal surface, which are difficult to measure, is avoided and replaced by one calibration parameter, which links simulation to experiments. The influence of variations in model parameters such as reflectivity and the heat absorption depth of the metal surface was investigated. The results such as the width and depth of the melt pool were shown to be robust.

The metal evaporation into the gas phase can be calculated based on the evaporation model of Klassen et al. [35] with approximations taken from Knight [36], an approach originally developed by Anisimov [37]. The mass flux of evaporated metal into the gas phase can be calculated by:

$$j_{net} = \Phi \cdot j_+, \quad j_+ = P_s \sqrt{\frac{m_A}{2 \pi k_B T_s}} \; , \tag{6}$$

where j_+ is the net mass flux, Φ the evaporation coefficient, m_A the atomic mass, k_B Boltzmann's constant, and T_s and P_s are temperature and pressure at the vapour side of the phase interface, respectively. The gas is treated as one phase with effective properties and the phase separation between Argon and evaporated metal gas are not taken into account. Absorption of laser energy by the gas plume is neglected.

P_s is calculated using the Clausius-Clapeyron equation given by [35]:

$$P_s = P_{atm} \cdot exp\left[-\frac{L_{vap,0} \cdot m_A}{k_B}\left[\frac{1}{T_s}\sqrt{1-\left(\frac{T_s}{T_{crit}}\right)^2} - \frac{1}{T_{boil}}\sqrt{1-\left(\frac{T_{boil}}{T_{crit}}\right)^2} - \frac{1}{T_{crit}}\left(sin^{-1}\left(\frac{T_s}{T_{crit}}\right) - \right.\right.\right.$$
$$\left.\left.\left. sin^{-1}\left(\frac{T_{boil}}{T_{crit}}\right)\right)\right]\right], \tag{7}$$

where $L_{vap,0}$ is the latent heat of vaporization ($T_s = 0$ K), $P_{atm} = 1$ bar and T_{crit} and T_{boil} are the critical and boiling temperature at one atmosphere, respectively.

The evaporation coefficient Φ gives the escaping atom/particle fraction (i.e. not scattered back or condensed onto the surface), which can be calculated by [35]:

$$\emptyset = \sqrt{2 \pi \gamma_v} \, Ma_{Kn}(T_s) \frac{\rho_{Kn}}{\rho_S} \sqrt{\frac{T_{KN}}{T_s}}, \tag{8}$$

where γ_v is the ratio of specific heats. In this work, $\gamma_v = 5/3$ for monoatomic gases is used. $Ma_{Kn}(T_s)$ is the flow Mach number at boundary of the Knudsen layer. The jump conditions across the Knudsen layer, T_{Kn}/T_s and ρ_{Kn}/ρ_s, are calculated using equations A1, A2 and A3 from Klassen *et al.* [35] and the approximation to the error function from Knight ([36] eq. 7). *A value of $Ma_{Kn}(T_s)= 0,2$ is used for all simulations, which gives a value of 0.46 for the evaporation coefficient Φ. Using the maximal value of $\Phi=0.82$ corresponding to $Ma_{Kn}(T_s)= 1$ instead was found to have little effect on the results.*

The momentum and energy equation source terms link the laser power absorption VHS_{laser} and the evaporation model to the continuum equations, given by:

$$\Delta m_{vap} = \frac{j_{net} * S_{VoF}}{\rho_{vap} * V_{cell}} \tag{9}$$

$$\Delta E_{vap} = \frac{j_{net} * S_{VoF} * L_{vap}(T_s)}{V_{cell}} + VHS_{laser} \tag{10}$$

Here, j_{net} is the net evaporation mass flux determined by Eq. (5), S_{VoF} is the surface of the metal represented by the VoF-surface separating melt and gas in each cell, ρ_{vap} the density of the evaporating gas, V_{cell} the cell volume of the mesh and VHS_{laser} the power density provided by the laser (see laser absorption model above). S_{VoF} is calculated assuming that the polyhedral cells can be approximated by a spherical shape (=> $r_{cell} = \sqrt[3]{3 V_{cell}/(4\pi)}$) and an estimation of the area of the cell segment given by the VoF-surface by $S_{VoF} =$

$(4 * f_m * (1 - f_m))^{0.45} * \pi * r_{cell}^2$. The latter gives an error smaller 3 % compared to a precise calculation of the segment surface, which can be neglected compared to the error introduced by the assumption of a spherical shape of each cell.

Particle spattering in LPBF processes occurs in a strongly fluctuating gas plume. The fluctuation could be caused by the variation in the distribution of particle size and the thickness of the powder bed [38] and in the laser beam energy output [39]. Due to the fluctuation of the field variables, an accurate estimation of the driving forces inducing particle motion is complicated by numerical instabilities. To our knowledge, there is no standard approach to estimate the scattering phenomenon in LPBF processes that overcomes these difficulties.

Investigating particle spattering by drag force due to an existing velocity difference between fluid and particles is the focus of this study. Drag force is the frictional force for a viscous flow derived by Stokes' law defined as:

$$F_d = \frac{1}{2} C_d \rho |u - u_{pt}|(u - u_{pt}) A_{pt} \qquad (11)$$

There are many drag models available to determine the fluid-solid drag forces in particulate flows. Most of the drag models introduce a drag force coefficient C_d to estimate the drag force. Because of its origin from Stokes' law, the drag coefficient in the above formula accounts for the feature around the individual particles. Therefore, for usual practices of various applications, it is to obtain the drag coefficient from correlations, typically derived from experiment or analytical studies. In general, C_d is treated as the function of Reynolds number Re. The effects of the shapes (sphere, disk and cylinder) of particles [40, 41], the sphericity [42] were taken into account for the determination of the drag coefficient. For multiphase flows in Eulerian approaches, surface tension effect [43] at the gas/liquid interfaces and the deformation of the bubbles [44] in liquid phase or the droplet in the gas phase were studied.

In the Lagrangian approach particles were treated as spheres with homogeneous material properties and various sizes. 3-dimensional trajectories were computed within the gas flow. A correlation analysis was carried out to obtain a suitable formula which adapts the results of the Lagrange calculation to the LPBF processes. Different drag coefficient models suitable for spherical, rigid particles were tested and the Schiller-Naumann drag model [45] found to give particle accelerations in agreement with the experimental findings (see sec. 4). The Schiller-Naumann model gives:

$$C_d = \begin{cases} \dfrac{24}{Re_{pt}} \left(1 + 0.15 Re_{pt}^{0.687}\right) & Re_{pt} \leq 10^3 \\ 0.44 & Re_{pt} > 10^3 \end{cases} \qquad (12)$$

$$Re_{pt} = \frac{\rho |u - u_{pt}| d_{pt}}{\mu} \qquad (13)$$

where Re_{pt} is the particle Reynolds number and d_{pt} the particle diameter.

Particle motion in the gas plume of a LPBF process has an impact on the surrounding fluid flow, and the affected local flow field will further influence the movement of the particle. To accurately capture the interaction between particle motion and gas flow, a two-way coupling approach becomes necessary to simulate particle spattering in LPBF processes. However, two-way coupling method assumes that the grid size for flow solver is larger than the particle size. This assumption fails in cases like this when simulation needs very fine gird density due to the demands of accurate flow solution in small length scale. The failing will bring large sources of momentum and energy to the small cells occupied by particles, and cause instability and inaccuracy in simulation.

To ensure correct coupling, when gird sizes are small comparing to particle sizes, a two-grid procedure is necessary. [46, 47] The two-grid method is a numerical option of source smoothing that clusters groups of contiguous cells together to create a virtual coarser grid for exchanging data. The size of the cell cluster is then independent on the underlying mesh size, but instead is based on the particle size. This ensures that particle sizes are always smaller than the cell size of the mesh used for coupling with the flow. The simulation uses these larger cells for calculating parcel interactions with the fluid phase. After calculating interactions, the simulation distributes the field variables, e.g., volume fraction contribution, momentum and energy source terms, and other transferred quantities, evenly across the component cells.

Simulation of evaporation, melting and solidification of metal powder in LPBF-processes with an Eulerian multiphase approach, combining particle tracking with a Lagrangian approach, is very computing time and computer resources demanding. A complete two-way two-grid Lagrangian approach applied to the whole powder bed is beyond the scope of this work, which focusses on melt pool dynamics, metal evaporation and their effect on the gas flow simulated by an Eulerian multi-phase approach. A simple Lagrangian approach is used to link experiments and Eulerian calculations (see Fig. 1). Therefore, the effect of the particle spattering on the gas flow was neglected to keep the numerical effort affordable. One-way coupling applied to only single particle was employed in the simulation. The influence of a single particle on the flow was supposed to be negligible at the starting instant of motion examined here. Because the two-grid method must be used together with the two-way coupling method, the two-grid method was transferred to a data-mapping procedure to determine the variables needed in equation (12) for an effective particle Reynolds number, and the drag coefficient in Schiller-Naumann drag model. The field variables of the fine grid used for Eulerian phases were mapped to a virtual coarser gird. The density, dynamic viscosity, velocity of the fluid in the local regions occupied by the particle were averaged under the coarser grid. A verification simulation was carried out to compare the one-way coupling and data-mapping procedure using the Schiller-Naumann model with the two-way coupling and two-grid procedure models [48–50]. The drag coefficients from the Schiller-Naumann model were found to lie within the values from the other models.

The data-mapping procedure with one-way coupling approach was used to track single particle motion in this work. The starting acceleration of particle from the powder bed was compared with the accelerations determined by the synchrotron X-ray imaging movies with a time resolution of 40,000 fps.

Tab. 1. Material and powder parameter		
	In718	Ti6Al4V
$T_{liquidus}$	1335 °C	1639 °C
$T_{solidus}$	1250 °C	1590 °C
L_{melt}	210 kJ/kg	275 kJ/kg
$T_{evaporation}$	2227 °C	2918 °C
T_{crit}	7395 °C	7617 °C
$L_{vap,0}$	6062 kJ/kg	9700 kJ/kg
$\mu_{ref}(Ar)$	$2.283 \cdot 10^{-5}$ Pa s	
$T_{ref}(Ar)$	100 K	
$\alpha(Ar)$	0.5	
Mean particle diameter	20 μm	29.5 μm

3. VALIDATION OF EULERIAN MULTI-PHASE SIMULATION

Melting, evaporation and solidification of IN718 and Ti6Al4V powder during single-track experiments were analysed by the particle resolving Eulerian approach. The IN718 powder was processed by DAP using their laboratory LPBF-machine. Temperature-dependent material parameters were taken from the STAR-CCM+ material database, validated by many casting simulations (see for example [31, 51], data for IN718 and Ti6Al4V mainly from [52]). The data was completed by evaporation, Argon viscosity and powder parameter. Tab. 1 gives the not temperature dependent parameter and Fig. 3c the particle size distribution.

The Argon viscosity parameter were calculated by a fit to measured data from [53]. A laser beam with Gaussian distribution (standard deviation = 20 μm) was modelled to melt the IN718 powder with laser powers for 142 to 285 W and laser speeds (v_{laser}) from 0.6 to 1.1 m/s. Using micrographs, the melt pool depth and width were analysed for different process settings.
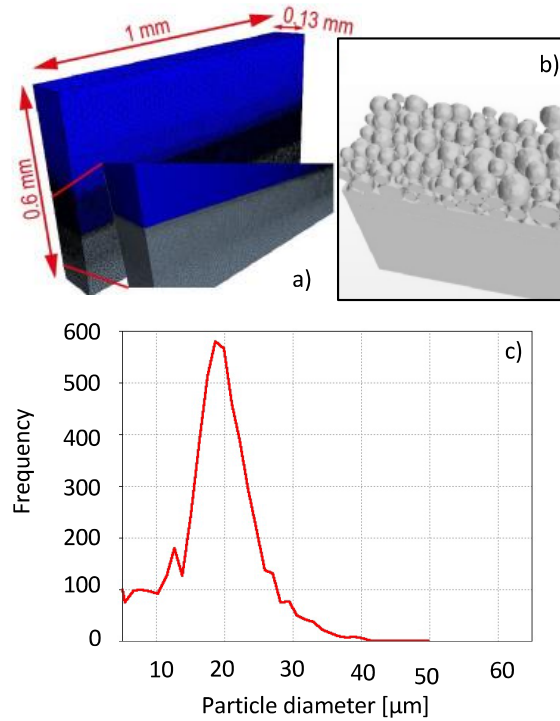

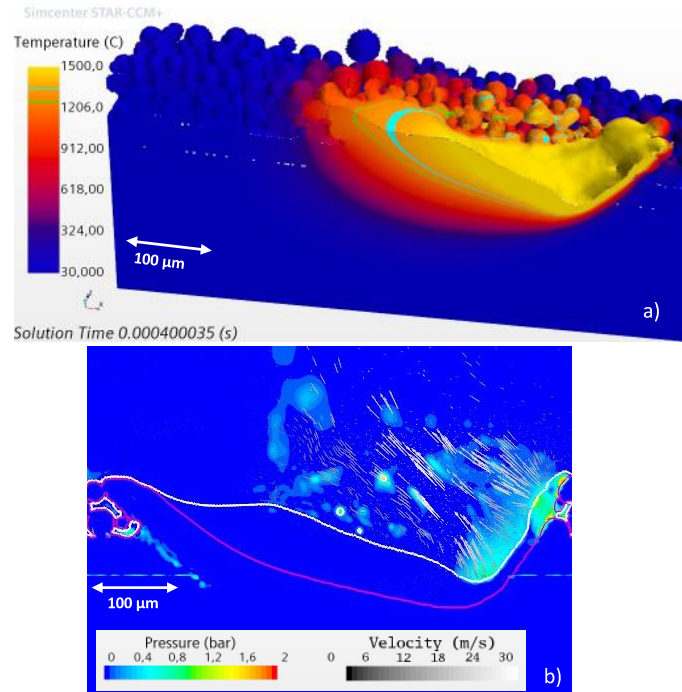Fig. 3: Geometry and mesh used a), initial powder bed b) and powder size distribution for the IN718 LPBF-process.

Fig. 4: Temperature on the melt surface a) and the distribution of pressure and gas velocity b) at steady-state conditions for the IN718 LPBF-process with P_{laser} = 194 W and laser speed 700 mm/s (I3 in Tab. 2).

Using a DEM simulation particles with the measured size distribution were placed above the substrate and drop by gravity down to the surface until a layer of the desired thickness was achieved. Position and diameter of each particle were transferred to the CV-based simulation of the LPBF-process by setting the VoF-function l_m describing the melt/gas interface to 1 inside the particle spheres and 0 outside. For the simulation, a 1000x130x600 μm^3 block was used taking advantage of the symmetry of the process along the build direction (symmetry plane at the centre of the melt pool in xz-plane). Fig. 3a shows the geometry of the block and the used 2.46 million cell polyhedral mesh with fine meshing in the powder layer region and beneath, where the melt pool is expected to develop. Fig. 3b gives the initial melt distribution. Powder layers of 60 μm and 90 μm thickness were investigated.

Tab. 2. Process parameter for IN718 simulations

ID	Material	layer thickness	Laser power	speed	line energy
		[μm]	[W]	[mm/s]	[J/mm]
I1	IN718	60 & 90	144	960	0.15
I2	IN718	60 & 90	194	1100	0.18
I3	IN718	60 & 90	194	700	0.27
I4	IN718	60 & 90	204	600	0.34
I5	IN718	60 & 90	244	600	0.41

Several simulations for different process parameters, summarized in Tab. 2, were performed for a 60 μm and 90 μm thick powder bed. Starting with an initial cold metal powder at room temperature and zero velocity of the Ar-gas above the powder, simulations were run until the melt pool depth and width fluctuates around a mean value (due to the powder particles' statistical distribution in the powder bed) and the simulation reached steady state process conditions. Fig. 4a) gives the temperature on the melt surface

and Fig. 4b) the distribution of pressure and velocity at steady-state conditions for P_{laser} = 194 W and v_{laser} = 700 mm/s. Fig. 5 compares the simulated melt pool depth (a+b) and width (c+d) for the 60 μm (a+c) and 90 μm (b+d) thick layer with the experimental findings at the DAP. An excellent agreement was achieved.
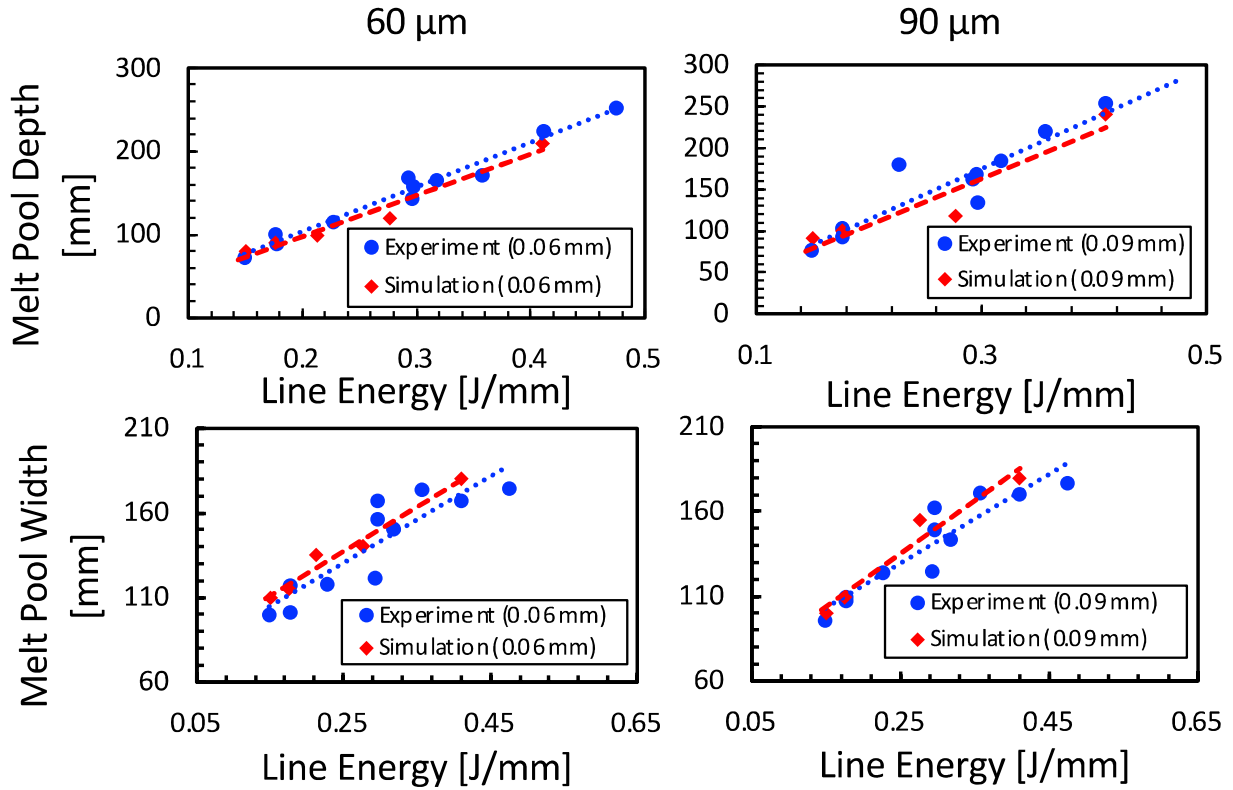

Fig. 5: Comparison of the simulated (red diamond, dashed line) melt pool depth (a+b) and width (c+d) for the 60 μm (a+c) and 90 μm (b+d) thick layer with the experimental findings (blue circle, dotted line) at the DAP.

This agreement could be achieved by linking the total power absorbed by the powder bed P_{total} to P_{laser} used in the experiments by a P_{total} dependent absorption coefficient as described in the theory section. Starting with a value of 0.33 for $P_{total} < 50$ W, which is typical for metal surfaces, the absorption coefficient rises linearly to 70 % for $P_{total} = 170$ W (see Fig. 6). Bayat et al. [16] reported a similar linear relation between absorption coefficient and laser power. Recent experimental studies combined with simulation on keyhole formation and absorption coefficient report a more complex relation between keyhole depth and shape and the absorption coefficient [21]. Such a detailed analysis is not possible based on the available data, and a linear dependence of the absorptivity between 0.3 and 0.7 gives a good approximation of the more complex behaviour.
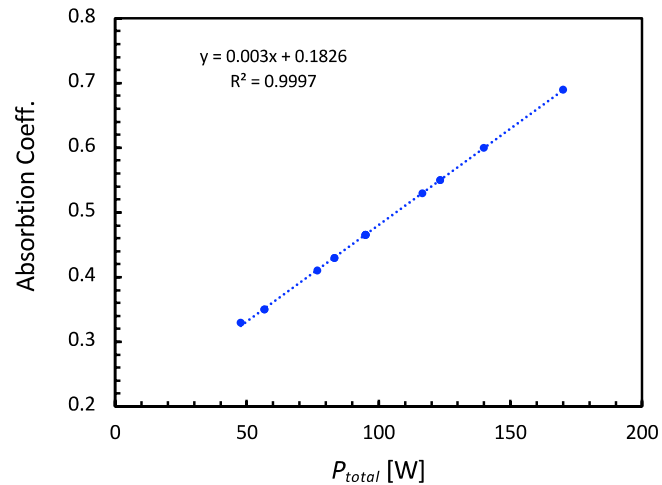
Fig. 6: Linear increase of the absorption coefficient as function of total energy P_{total}.

The synchrotron experiments were performed using a Ti6Al4V powder with a size distribution between 10 – 80 μm measured using a Mastersizer
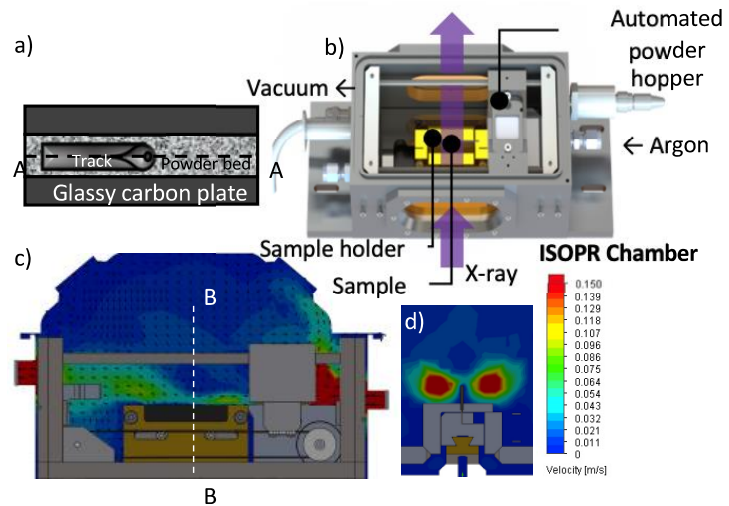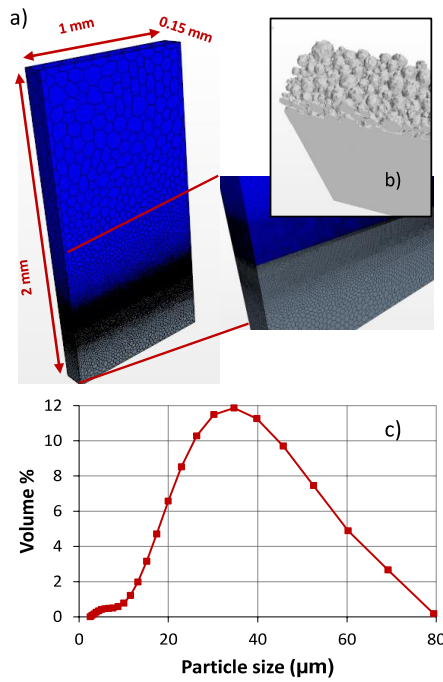
Fig. 7: Schematic of the ISOPR additive manufacturing machine for capturing the LBPF process using synchrotron imaging.

a) 1 mm 0.15 mm 2 mm

b)

c)

Volume % vs *Particle size (μm)*

2000 laser diffractometer (see

Fig. 8c). The powder was essentially spherical with a D50 of 29.5 μm, typically for LPBF and a powder layer thickness of 60 μm. A laser beam with Gaussian distribution (standard deviation = 14 μm) was modelled to melt the Ti6Al4V powder with laser powers between 150 W and 200 W and a laser speeds from 0.1 to 0.4 m/s.

The Ti6Al4V powder was processed by an *in situ* and *operando* laser additive manufacturing process replicator (ISOPR) at the X-ray radiography facility (ID19 imaging beamline) at the European Synchrotron Radiation Facility (ESRF) in Grenoble, France [5]. The ISOPR system, documented by Leung et al. [9] operates with an industrially typical 50 mm focused TEM00 spot [51] and was integrated onto the X-ray beam producing a radiographic video of the process. A 200 μm thick LuAg: Ce scintillator and FASTCAM SA-Z 2100K camera captured the radiographs at 40,000 fps and 12.6 μs exposure time.

The simulation approach follows exactly the one used for the IN718 powder. Temperature-dependent material parameters were taken from the STAR-CMM+ material database and completed by evaporation and powder parameter given in

Tab. 3. Process parameter for Ti6Al4V simulations

ID	layer thickness	laser power	speed	line energy
	[μm]	[W]	[mm/s]	[J/mm]
T1	60	151	600	0.25
T2	60	200	400	0.50
T3	60	175	285	0.61
T4	60	200	285	0.70
T5	60	175	200	0.88
T6	60	204	200	1.02
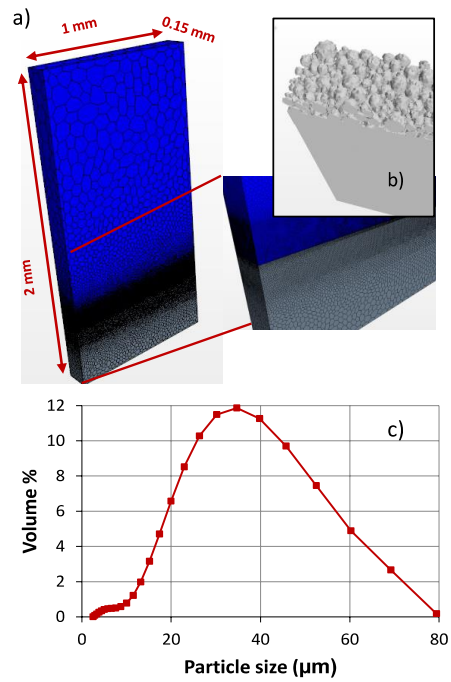
Tab. 1 and the particle size distribution in

Fig. 8c. A DEM-simulation was used to generate a powder bed with the particle size distribution measured for the Ti6Al4V powder. A 1000x150x2000 μm^3 block was used with a fine mesh resolution at the position of the powder bed and the expected melt pool. The height of the block was enlarged to 2 mm to allow a free gas flow above the powder bed as found in the experiments since these simulations are used to compare the Lagrangian motion of spattered particles with the experimental findings using synchrotron
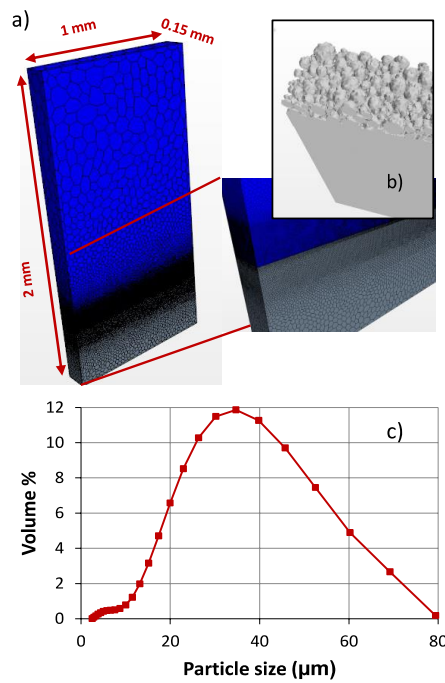
X-ray imaging.

Fig. 8 shows the geometry and mesh a) and the initial particle distribution from DEM simulation b). Again,

symmetry was used to reduce the block size by a factor of two using an *xz*-symmetry plane along the laser track.
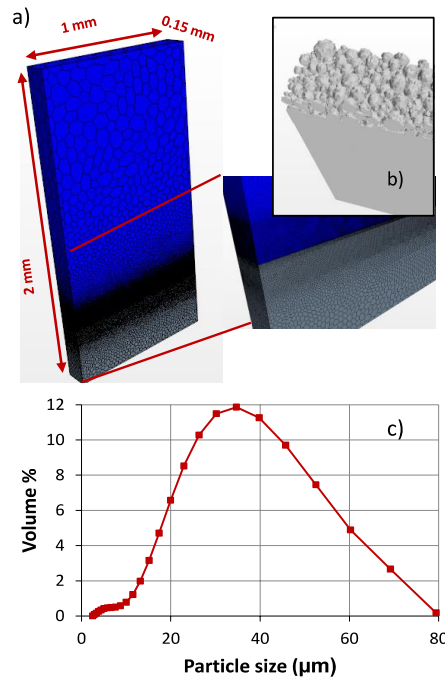
Fig. 8: Geometry and mesh used a), initial powder distribution from DEM simulation b) and powder size distribution c) for the Ti6Al4V LPBF-process.
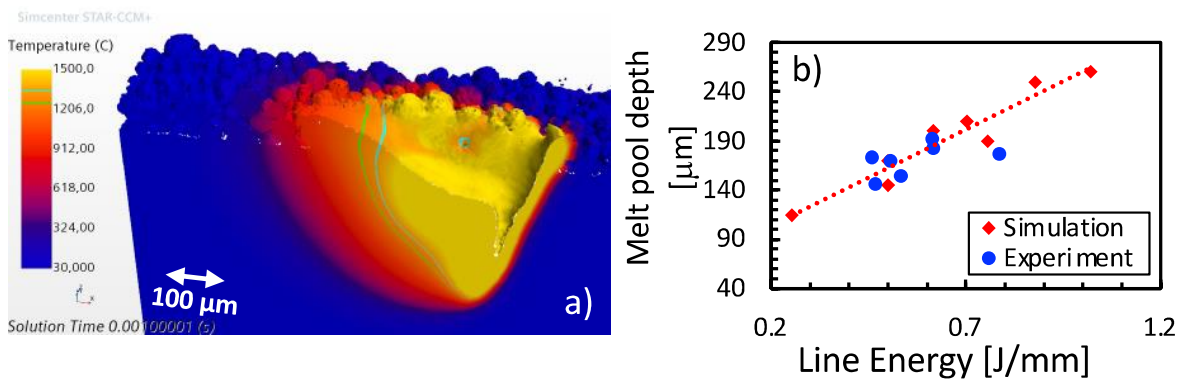

Fig. 9: a) Temperature on the melt surface for theTi6Al4V LPBF-process with P_{laser} = 200 W and v_{lase} = 285 mm/s (T4 in Tab. 3). Turquoise is the liquidus and green the solidus temperature line. b) Simulated melt pool depth (red diamond) versus experimental findings (blue circle) for different line energies.

Several simulations for different process parameters, summarized in Tab. 3, were performed for a 60 μm thick powder bed. Fig. 9 shows the temperature on the melt surface a) at steady-state conditions for the Ti6Al4V LPBF-process and compares the simulated with the measured melt pool depth b). Using the same P_{total} dependent absorption coefficient as for the IN718-process a good agreement could be found.
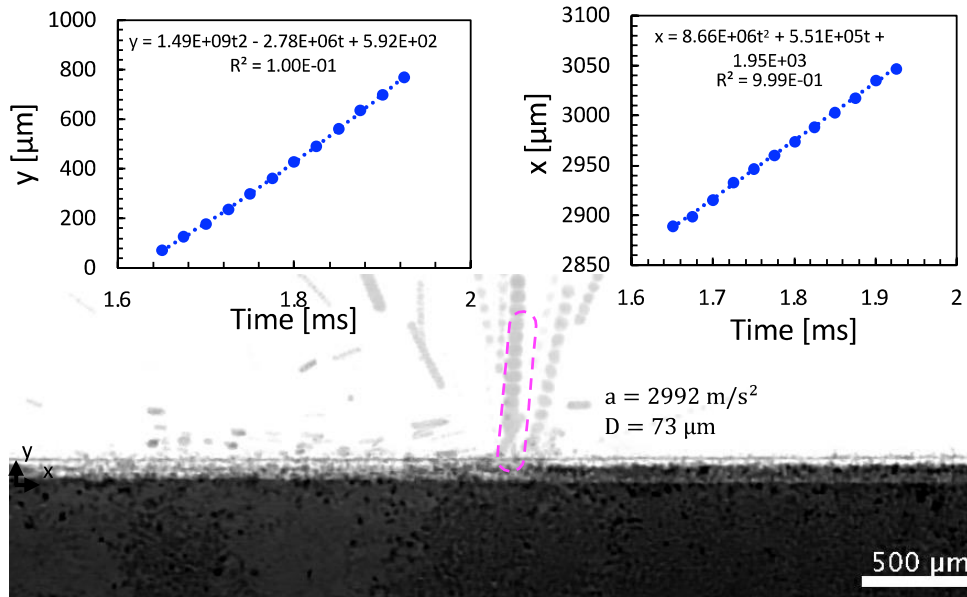
4. PARTICLE SCATTERING

Fig. 10: Scattering of a 73.25 mm particle and derived movement in x (right inset) and y (left inset) direction. By fitting a linear and a quadratic polynomial, a velocity of 0.62 m/s and acceleration of 2992 m/s² in the x-y-plane could be calculated.

Synchrotron X-ray imaging movies with a high time resolution of 40,000 fps obtained by the ISOPR LBPF process replicator at ESRF (European Synchrotron Radiation Facility) were used to analyse the spattering of particles during the Ti6Al4V LPBF-process. Fig. 10 gives typical results for a laser power of 200 W and speed of 285 mm/s showing several particles accelerated out of the powder at different angles. From the trajectory, the positions in x and y-direction could be determined, as the insets with position vs time plots show for a 73 μm particle. (See inset left for *y*-direction and inset right for *x*-direction). By fitting a linear and quadratic polynomial to the position vs time plots a velocity of 0.62 m/s and acceleration of 2992 m/s² in the *x-y*-plane could be calculated.
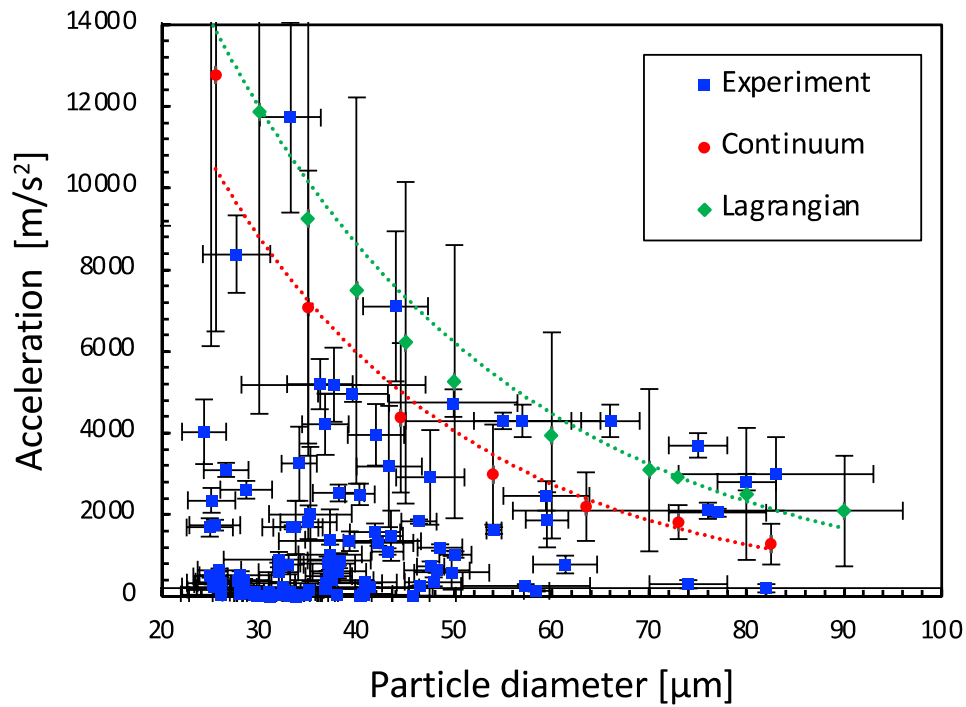
Fig. 11: Experimentally determined particle acceleration as a function of the particle size (blue square), Lagrangian simulation (green diamond) and continuum calculation (red circle) for a Ti6Al4V-process (T4: P_{laser} = 200 W and v_{laser} = 285 mm/s). An exponential law was fit to the Lagrangian and continuum data.
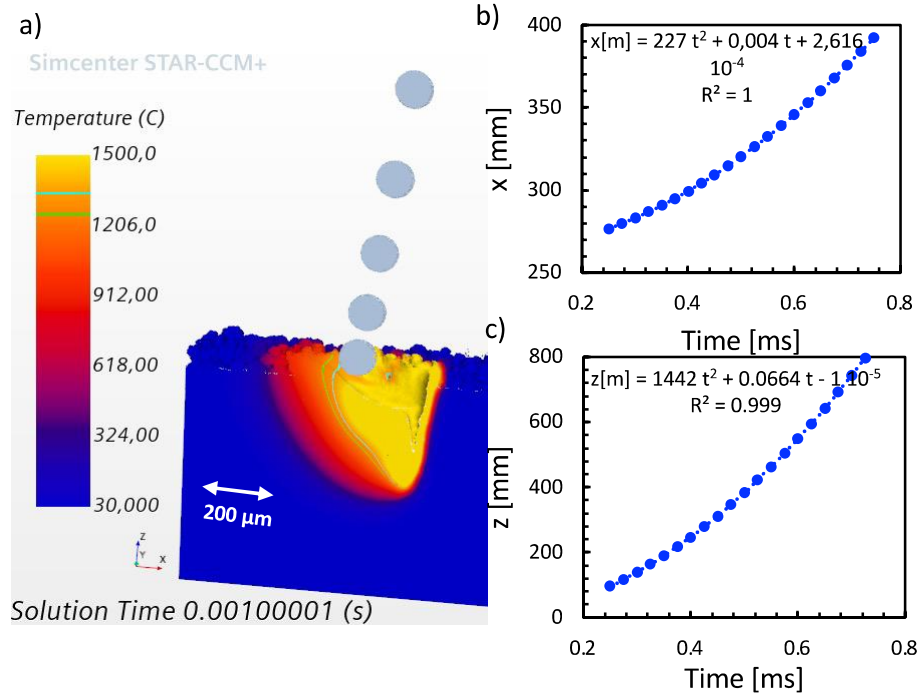
Fig. 12: Visualization of the Lagrangian simulation of a 73 μm particle and derived movement in z (e) and x (f) direction.

A series of trajectories were analysed in the same way. Fig. 11 gives the acceleration in the *x*-*y*-plane as a function of the particle size. Since the acceleration in the vertical *z*-direction cannot be obtained by synchrotron radiation, the determined accelerations can be significantly larger than the given numbers.

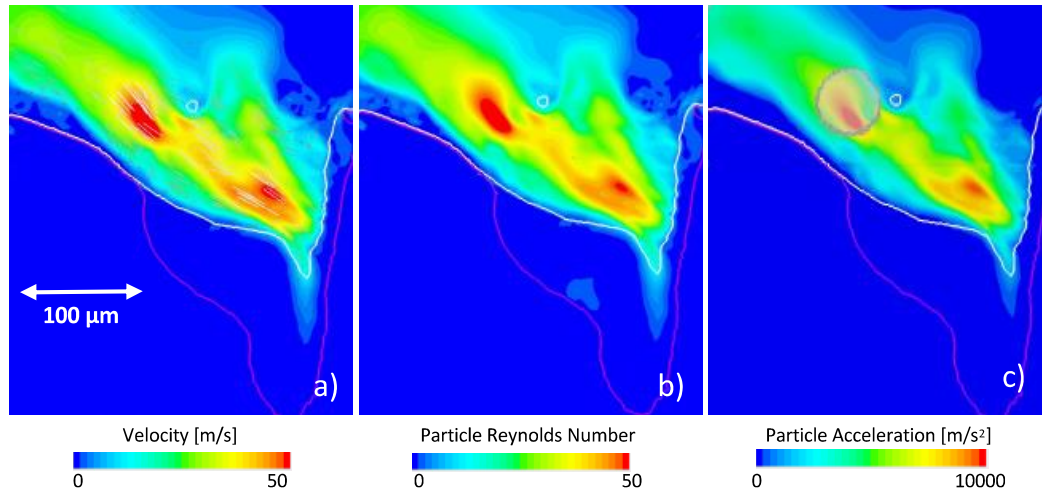| Velocity [m/s] | Particle Reynolds Number | Particle Acceleration [m/s²] |
| 0   50 | 0   50 | 0   10000 |

Fig. 13: Velocity field a), the particle Reynolds number b) and the drag force acceleration c) for a 73 μm particle in the Ti6Al4V-LPBF-process with P_{laser} = 200 W and v_{laser} = 285 mm/s (T4 in Tab. 3).

The Lagrangian approach described in section 2 was used to model the scattering of particles based on the velocity field of the Eulerian multi-phase simulation for the Ti6Al4V LPBF-process also using P_{laser} = 200 W and v_{lase} = 285 mm/s. Particles of different size were placed in the velocity field and their movement followed similar to the experimental analysis. Fig. 12 visualizes a typical movement for a 73 μm particle as a result of the Lagrangian simulation by a 73 μm sphere at 5 positions with a time difference of 0.1 ms. By a linear and a quadratic fit to the trajectory in *x*- and *z*-direction (*z*-direction in the simulation corresponds to the *y*-direction in the experiments), a velocity of 0.5 m/s and an acceleration of 2920 m/s^2 could be determined. Obviously, using the velocity field from Eulerian calculation in the Lagrangian approach leads to particle trajectories, which fit to those observed in synchrotron experiments (Fig. 10). A series of Lagrangian particle trajectories were analysed for particle diameter between 25 μm and 90 μm. Particles accelerated out of the keyhole are likely to lead to critical defects, if they reach high velocities and fly far into powder bed regions that have not yet been processed. Therefore, Lagrangian trajectories starting in the high gas velocity region of the keyhole and gaining high velocities were analysed by simulation. Such a selection is not possible in experiments and particles may be accelerated at different positions inside the gas flow, often with lower gas velocities. Consequently, the particle accelerations from Lagrangian simulations at high gas velocity regions should mark the maximal values of particle accelerations found in experiments. This relation was, indeed, observed as Fig. 11 demonstrates: the accelerations calculated by the Lagrangian approach agree with the fastest particle acceleration found in the experiments. Here we focus on the Eulerian multi-phase approach and the results of the synchrotron experiments and Lagrange simulation demonstrate that the Eulerian multi-phase approach gives fields describing the evaporation gas plume, from which the acceleration and scattering of particles can be calculated in good agreement with experimental findings.

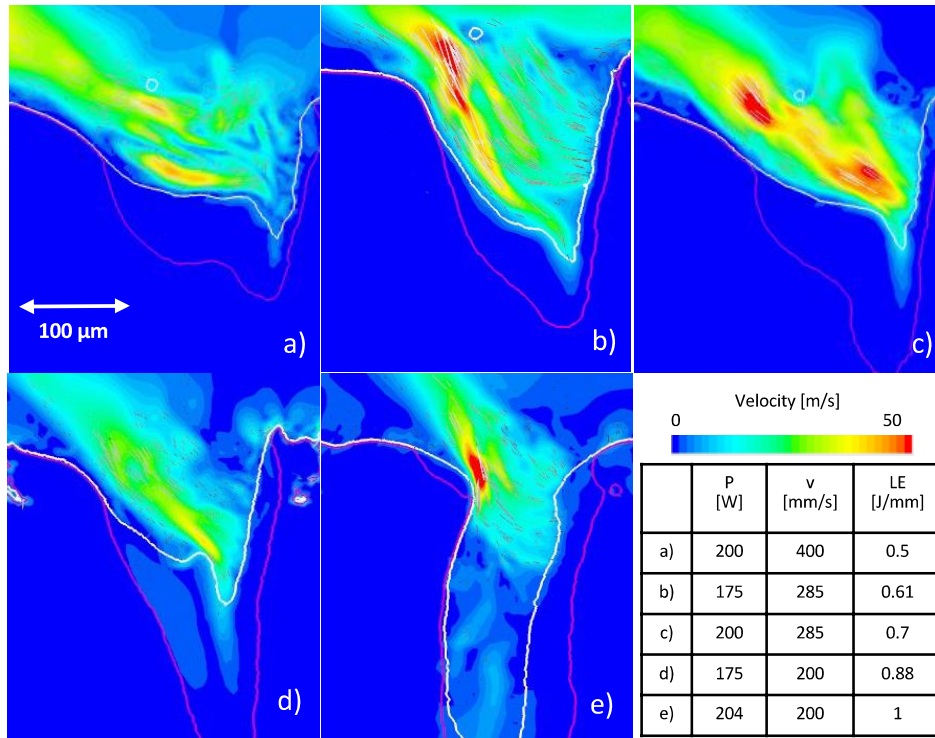|	P [W]	v [mm/s]	LE [J/mm]
a)	200	400	0.5
b)	175	285	0.61
c)	200	285	0.7
d)	175	200	0.88
e)	204	200	1

Fig. 14: Velocity field of five Ti6Al4V-processes with different laser power and speed and increasing line energy from a) to e) using process parameter T2 - T6 from Tab. 3.

To analyse the effect of process parameters on the scattering, an approach based only on the Eulerian multi-phase calculations is useful to avoid the long computation times of the Lagrangian approach. Based on the velocity field, the temperature-dependent gas density, viscosity, and the particle diameter the particle Reynolds number Re_{pt} can be calculated using eq. 8. From this, the drag force acceleration can be derived using the Schiller-Naumann drag force model (eq. 6 and 7). Fig. 13 shows the velocity field a), the particle Reynolds number b) and the drag force acceleration c) for the Ti6Al4V-LPBF-process with $P_{laser} = 200$ W and $v_{laser} = 285$ mm/s for a particle with 73 µm diameter. The region above the white line is gaseous, the region below the magenta line solid. The Reynold number and drag force acceleration fields follow closely the velocity distribution. Highest gas velocities, particle Reynolds numbers and particle accelerations are found towards the end of the keyhole. The circle in the acceleration plot shows the size of a 73 µm particle positioned at the top of the powder bed at the position of highest gas velocities. The particle size is significantly larger than the mesh size and the acceleration of the particle was calculated by averaging the acceleration field over the particle area. Since the gas velocities in the fast gas stream regions are more than one order of magnitude higher than the particle velocities, the later was neglected in the calculation of Re_{pt} and particle acceleration $a_{pt} = F_d/m$. In reality, a particle of this size will influence the velocity field. Recently, this influence from the particle back to the gas flow was modelled by a two-way coupling between a finite volume descriptions of gas flow and vapour jet to a discrete element model of the particle movement without a treatment of the melt pool and powder bed [30]. This work focusses on melt pool dynamics, metal evaporation and their effect on the gas flow. The effect of the particle spattering on the gas flow was neglected to keep the numerical effort affordable.
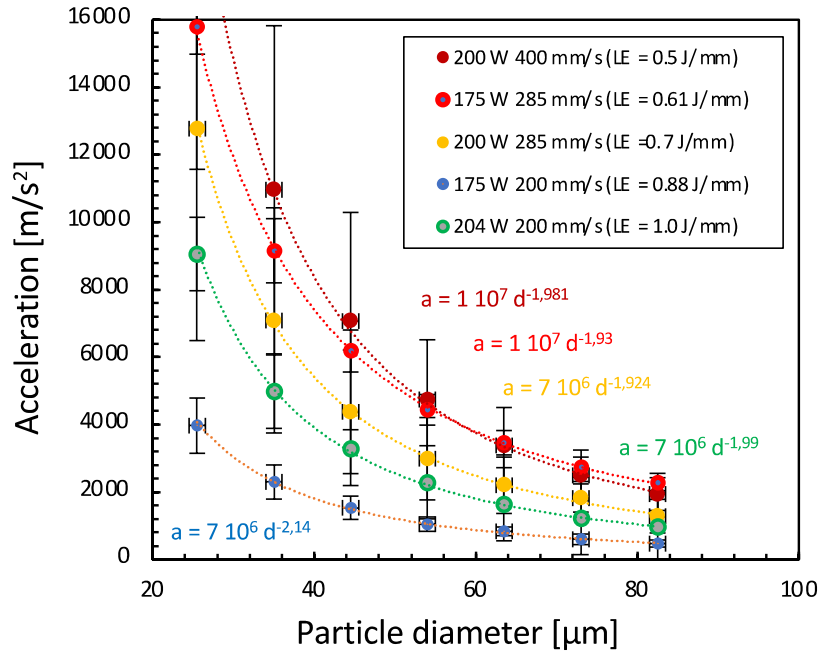
Fig. 15 Particle diameter d_{pt} dependence of the particle acceleration a_{pt} for the simulations for the Ti6Al4V process with different laser power / speed: 200 W / 400 mm/s (dark red, T2), 175 W / 285 mm/s (red, T3), 200 W / 285 mm/s (orange, T4), 175 W / 200 mm/s (blue, T5) and 204 W / 200 mm/s (green, T6). A potential law can fit all three curves with an exponent near -2.
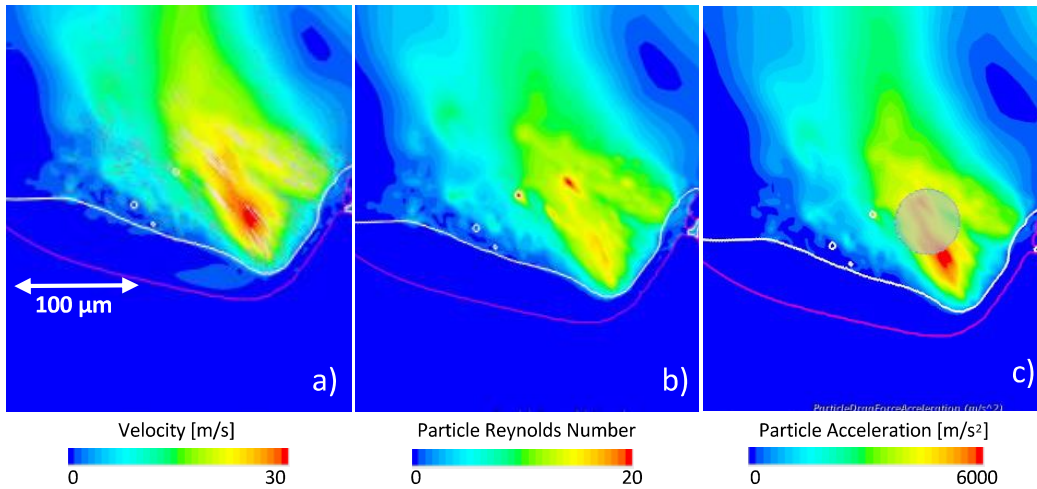

Fig. 16: Velocity field a), the particle Reynolds number b) and the particle acceleration c) for the IN718-LPBF-process with $P_{laser} = 194$ W and $v_{laser} = 700$ mm/s (I3 from Tab. 2) and a spherical particle with diameter 54 μm.

For different particle sizes and positions in the gas stream, the particle acceleration was determined. In Fig. 11, the mean values of the accelerations are plotted as red points with the standard deviation as error bar in comparison to the Lagrangian and experimental findings. In good agreement with the results from the

Lagrangian approach, the data points from Eulerian multi-phase simulation agree with the maximal values of the measurement. As in the Lagrangian approach, in the Eulerian multi-phase simulation, the particles were placed in the maximum velocity field gaining the highest possible accelerations found in experiments.

5. INFLUENCE OF PROCESS PARAMETERS ON PARTICLE ACCELERATION

In this section, velocity field distributions calculated using the Eulerian multi-phase approach and the deduced particle accelerations are used to analyse the influence of process parameter on the particle scattering. Fig. 14 shows the velocity field for a 73 μm particle for five different laser powers and laser speeds combinations with increasing line energy from 0.5 J/mm up to 1 J/mm. As in Fig. 13 the region above the white line is gaseous, the region below the magenta line solid. The depth of the melt pool (magenta line) increases with increasing line energy in good agreement with the linear relation between the line energy and the melt pool depth shown in Fig. 9 b). The relations between velocity magnitude and line energy are more complex and depend significantly on the melt pool and keyhole shape. The velocity field shows regions with 50 m/s for parameter combinations with line energies of 0.61 J/mm, 0.7 J/mm and 1 J/mm. The results for the line energies 0.5 J/mm and 0.88 J/mm reveal lower maximal velocities.

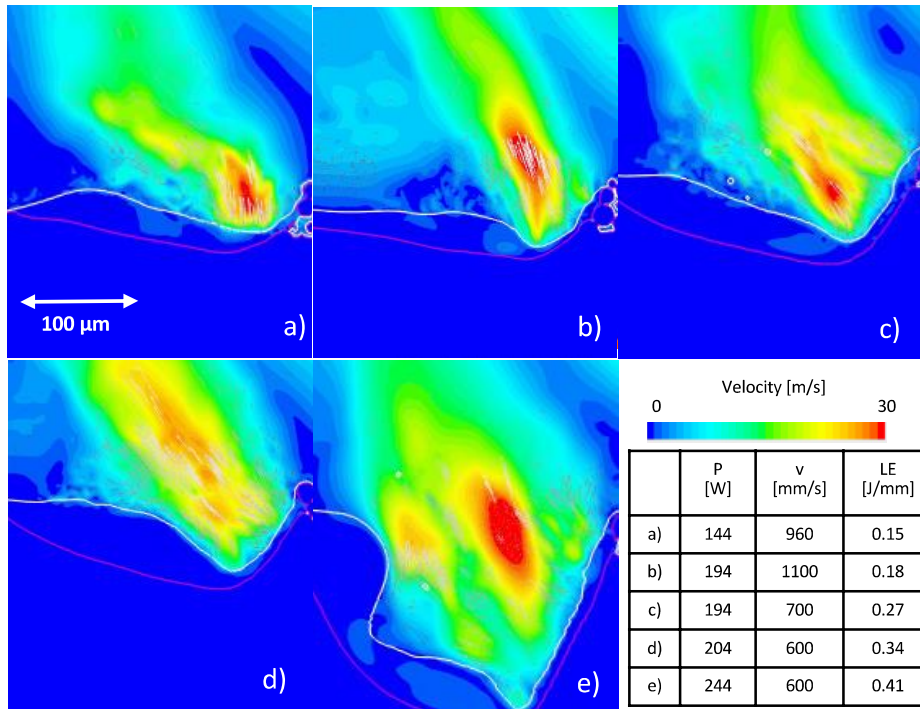|	P [W]	v [mm/s]	LE [J/mm]
a)	144	960	0.15
b)	194	1100	0.18
c)	194	700	0.27
d)	204	600	0.34
e)	244	600	0.41

Fig. 17 Velocity field of five IN718-processes with different laser power and speed and increasing line energy from a) to e) (process parameter I1-I5 from Tab. 2).

This more complex behaviour is visible in Fig. 15, where the particle diameter dependences of the particle acceleration a_{pt} are plotted for the five process parameter combinations. For three particle positions at 100 μm, 200 μm and 300 μm above the powder bed a_{pt} was calculated and the mean value and standard deviation plotted. The d_{pt} dependences follow a potential law with an exponent near -2 in good agreement with theoretical consideration: eq. 6 gives: $a_{pt} = F_d / m \sim C_d A_{pt} / V_{pt} \sim C_d / d_{pt}$ and eq. 7 for $Re_{pt} < 30$ ($1 > 0.15 Re_{pt}^{0.687}$) $C_d \sim 1/d_{pt}$. Consequently, $a_{pt} \sim d_{pt}^{-2}$ should hold. Comparing the points for the same particle size, no clear line energy dependence can be found and higher line energies seem to be connected with lower particle accelerations. This unexpected behaviour can be explained by the keyhole shape: for deep keyholes

the hot spot with large metal evaporation is deep inside the keyhole and spatially separated from the top of the keyhole, where particles can be accelerated and leave the powder bed.

The analysis of the influence of the process parameters on the particle acceleration was applied in the same way to the IN718 process. Fig. 16 gives the velocity, particle Reynolds number and particle acceleration fields for a particle with 54 μm diameter for the process with $P_{laser} = 194$ W and $v_{laser} = 700$ mm/s. Similar to Fig. 13 for the Ti6Al4V process, the fields Reynold's number and drag force acceleration follow the velocity distribution.

Fig. 17 shows the velocity field for a 54 μm particle and a powder bed thickness of 60 μm for five different laser powers and laser speeds combinations with increasing line energy from 0.15 J/mm to 0.41 J/mm. The depth of the melt pool (magenta line) increases with increasing line energy in good agreement with the linear relation between the line energy and the melt pool depth shown in Fig. 5a) +c). For the process parameter combinations with line energies below 0.34 J/mm the shallow keyhole (conduction mode) follows the melt pool geometry. Only with a line energy of 0.41 J/mm, a deeper keyhole forms and the keyhole shape get more complex. The process enters the transition mode.

Similar to Fig. 15, Fig. 18 gives the particle diameter d_{pt} dependence of the particle acceleration a_{pt} for the five process parameter combinations and a power-law dependence with an exponent close to -2 can be observed. In contrast to the findings for the Ti6Al4V process, the particle acceleration for the IN718 process shows a line energy dependency with increasing particle accelerations for higher line energies, the process is in the conduction mode.
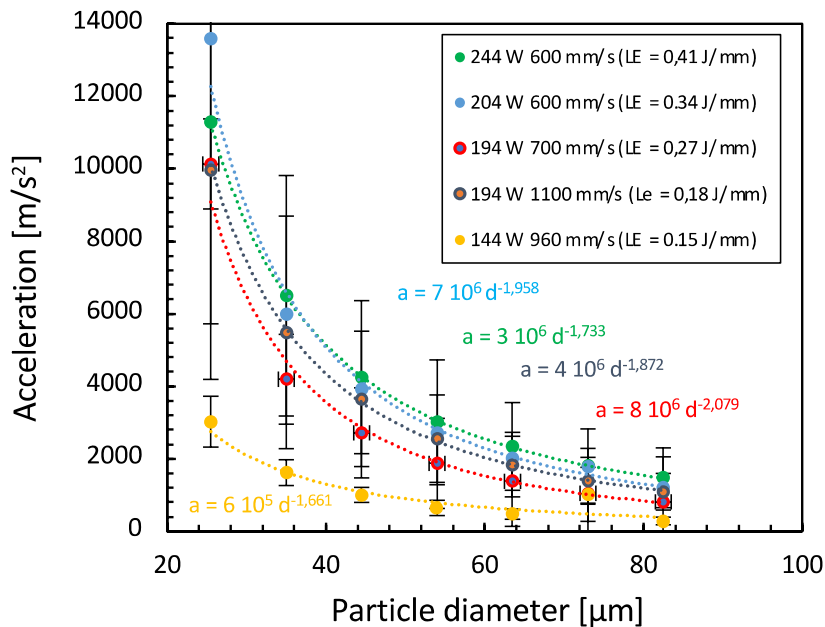

Fig. 18: Particle diameter dependence of the drag force acceleration for the simulations of IN718 processes with different laser power / speed: 244 W / 600 mm/s (green, I5), 204 W / 600 mm/s (blue, I4), 194 W / 700 mm/s (red, I3), 194 W / 1100 mm/s (black, I2) and 144 W / 960 mm/s (yellow, I1). A potential law can fit all three curves with an exponent from 1.6 to 2.1.
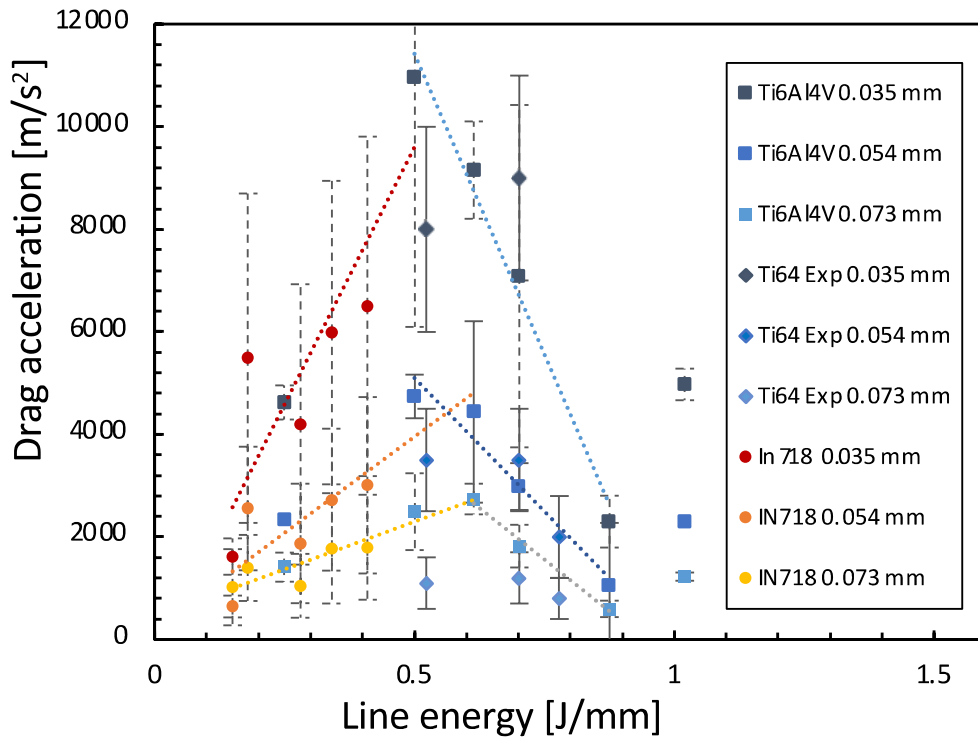
Fig. 19: Investigation of possible line energy dependencies of the drag force acceleration for Ti6Al4V-processes (rhombus experimental, squares and circles simulation results) with particle sizes 35 μm (dark blue), 54 μm (blue) and 73 μm (light blue) and IN718-processes with particle sizes 35 μm (red), 54 μm (orange) and 73 μm (yellow).

Fig. 19 gives a combined analysis of the line energy dependence of the particle acceleration for the Ti6Al4V (T1-T6 from Tab. 3) and IN718 (I1-I5 from Tab. 2) process. For low line energies (conduction mode), a linear fit to the acceleration vs line energy data of the IN718 process is possible. Higher line energies lead to more melt evaporation, higher gas stream velocities and consequently, higher particle accelerations. Interestingly, the low line energies data (LE < 0.61 J/mm) of the Ti6Al4V-process fit to the found linear correlation of the IN718-process. This result is not expected because IN718 and Ti6Al4V have different material properties. Two effects seam to compensate: IN718 particles are about 1.85 times heavier than Ti6Al4V particles, and higher gas velocities are required to achieve a similar acceleration. Heating IN718 to boiling temperature requires about 0.6 times less energy than Ti6Al4V because IN718 has a lower boiling temperature and lower latent heat of vaporization. Apparently, the combination of higher kinetic energy of the gas cloud and heavier particles in the case of IN718 metal vapour plume leads to a similar maximal acceleration as the combination of lighter particles and gas plume with lower kinetic energy. For LE > 0.61 a linear decrease of the maximum particle acceleration can be found, which was, to our knowledge, not yet reported. The results are supported by the results from synchrotron experiments analysed in Fig. 11. These results (P_{laser}= 200 W, v_{laser} = 285 mm/s, LE = 0.7 J/mm) and results from two additional synchrotron experiments (Plaser= 150 W, vlaser = 193 mm/s, LE = 0.52 J/mm, Plaser= 200 W, vlaser = 383 mm/s, LE = 0, 78 J/mm) were added to simulation data in Fig. 19. The synchrotron results yield a similar maximal acceleration when increasing LE from 0.52 J/mm to 0.7 J/mm and reduction of the maximal acceleration when LE is further increased to 0.78 J/mm, very similar to the reduction found as a result of the simulations. In the authors view, the unexpected decrease of the maximal acceleration with increasing line energy can be associated with the deepening of the keyhole, resulting in a spatial distance between gas evaporation

region in the keyhole and the region with highest particle acceleration at the top end of the keyhole. For line energies above 1 J/mm, when a deep keyhole forms and the process enters keyhole mode, the dependence changes again and the particle acceleration increases with increasing line energy.

6. CONCLUSIONS AND OUTLOOK

Melting, evaporation and solidification of the metal powder in LPBF-processes are simulated using an Eulerian multiphase approach. The methodology was extended via particle acceleration models based on a simple Lagrangian model in order to analyse the particle spattering with a moving laser source. The methodology was applied to two LPBF processes.

- Ti6Al4V powder with average particle size of 29.5 µm and a powder layer thickness of 100 µm. The particle spatter dynamics of this process was analysed by synchrotron X-ray imaging experiments.
- IN718 powder with average particle diameter of 20 µm and powder layer thicknesses of 60 µm and 90 µm. Melt pool depth and width were analysed by micrograph for the comparison with simulation results.

To compare particle scattering with trajectories seen in synchrotron X-ray images of the Ti6Al4V-process, particle trajectories were calculated based on the gas velocity fields from Eulerian simulation using Lagrangian particle simulation with a Schiller-Naumann drag force model. Particle velocities and accelerations from Lagrangian simulation and experiments were found to be in good agreement.

In order to avoid numerical laborious Lagrangian calculations, a direct method to compare an Eulerian multiphase simulation with synchrotron X-ray experiments was introduced and validated: particle accelerations were calculated from the gas velocity distribution using the Schiller-Naumann drag force model by averaging the calculated acceleration field over the particle volume. By this approach, particle accelerations could be calculated in agreement with the experimental findings and the Lagrangian results.

This direct method based just on Eulerian multiphase calculations was used for a parametric study of the effect of process parameter laser power and laser speed on the particle acceleration and, consequently, the particle spattering. The main findings are:

- For low line energies (LE < 0.5 J/mm, conduction mode) the particle acceleration increases linearly with line energy.
- The same linear relation could describe results for IN718 and Ti6Al4V-powder. Here, the higher weight of IN718particles seems to be compensated by higher gas velocities due a lower energy consumption to evaporate IN718.
- For higher line energies up to 1 J/mm (transition mode), a linear decrease of the particle acceleration could be observed in experimental and simulation results. This can be associated with the transition from a shallow depletion region to a deep keyhole resulting in a spatial separation of evaporation region and the area important for particle acceleration.
- The change of the keyhole shape with increasing line energy is important for the strength of particle spattering. Front and back of the keyhole show a different behaviour.
- For higher line energies above 1 J/mm (keyhole mode), increasing particle acceleration with increasing line energy can be observed.
- The particle size dependence of the particle acceleration follows a potential law with exponents close to -2 in good agreement with theoretical considerations.

These results suggest that in order to combine high part density with low spattering LPBF processes should ideally operate in the transition from transition to keyhole mode. A more detailed analysis of this interaction and the application of the method to additional process parameters such as the gas velocity over the powder bed, hatching strategies and powder particle distributions are planned. The newly developed simulation method, which combines a multi-phase Euler approach with a metal evaporation model and an acceleration of particles by a drag force can provide valuable information about the interaction of process parameters, keyhole formation and particle spattering in LPBF processes.

7. ACKNOWLEDGEMENTS

REFERENCES

[1]   S.H. Huang, P. Liu, A. Mokasdar, L. Hou, Additive manufacturing and its societal impact: a literature review, The International Journal of Advanced Manufacturing Technology. 67 (2013) 1191–1203.

[2]   M. Schmidt, M. Merklein, D. Bourell, D. Dimitrov, T. Hausotte, K. Wegener, L. Overmeyer, F. Vollertsen, G.N. Levy, Laser based additive manufacturing in industry and academia, CIRP Annals. 66 (2017) 561–583.

[3]   P. Hanzl, M. Zetek, T. Bakša, T. Kroupa, The Influence of Processing Parameters on the Mechanical Properties of SLM Parts, Procedia Engineering. 100 (2015) 1405–1413.

[4]   G. Egger, P.E. Gygax, R. Glardon, N.P. Karapatis, Optimization of powder layer density in selective laser sintering, 10th Solid Freeform Fabrication Symposium (SFF). (1999) 255–263. http://infoscience.epfl.ch/record/153069.

[5]   Y. Chen, S.J. Clark, C.L.A. Leung, L. Sinclair, S. Marussi, M.P. Olbinado, E. Boller, A. Rack, I. Todd, P.D. Lee, In-situ Synchrotron imaging of keyhole mode multi-layer laser powder bed fusion additive manufacturing, Applied Materials Today. 20 (2020). https://doi.org/10.1016/j.apmt.2020.100650.

[6]   L. Sinclair, C.L.A. Leung, S. Marussi, S.J. Clark, Y. Chen, M.P. Olbinado, A. Rack, J. Gardy, G.J. Baxter, P.D. Lee, In situ radiographic and ex situ tomographic analysis of pore interactions during multilayer builds in laser powder bed fusion, Additive Manufacturing. 36 (2020). https://doi.org/10.1016/j.addma.2020.101512.

[7]   T.M. Mower, M.J. Long, Mechanical behavior of additive manufactured, powder-bed laser-fused materials, Materials Science and Engineering A. 651 (2016) 198–213. https://doi.org/10.1016/j.msea.2015.10.068.

[8]   A. Yadollahi, N. Shamsaei, Additive manufacturing of fatigue resistant materials: Challenges and opportunities, International Journal of Fatigue. 98 (2017). https://doi.org/10.1016/j.ijfatigue.2017.01.001.

[9]   C.L.A. Leung, S. Marussi, R.C. Atwood, M. Towrie, P.J. Withers, P.D. Lee, In situ X-ray imaging of defect and molten pool dynamics in laser additive manufacturing, Nature Communications. 9 (2018) 1–9. https://doi.org/10.1038/s41467-018-03734-7.

[10]   S.A. Khairallah, A. Anderson, Mesoscopic simulation model of selective laser melting of stainless steel powder, Journal of Materials Processing Technology. 214 (2014) 2627–2636.

[11]   W.E. King, A.T. Anderson, R.M. Ferencz, N.E. Hodge, C. Kamath, S.A. Khairallah, A.M. Rubenchik, Laser powder bed fusion additive manufacturing of metals; physics, computational, and materials challenges, Applied Physics Reviews. 2 (2015) 041304. https://doi.org/10.1063/1.4937809.

[12]   F.J. Gürtler, M. Karg, M. Dobler, S. Kohl, I. Tzivilsky, M. Schmidt, Influence of powder distribution on process stability in laser beam melting: Analysis of melt pool dynamics by numerical simulations, 25th Annual International Solid Freeform Fabrication Symposium; An Additive Manufacturing Conference, SFF 2014. (2014) 1099–1117.

[13]   M. Megahed, H.W. Mindt, N. N'Dri, H. Duan, O. Desmaison, Metal additive-manufacturing process and residual stress modeling, Integrating Materials and Manufacturing Innovation, 2016. https://doi.org/10.1186/s40192-016-0047-2.

[14]   J. Zielinski, H.W. Mindt, J. Düchting, J.H. Schleifenbaum, M. Megahed, Numerical and Experimental Study of Ti6Al4V Components Manufactured Using Powder Bed Fusion Additive Manufacturing, Jom. 69 (2017) 2711–2718. https://doi.org/10.1007/s11837-017-2596-z.

[15]   J. Zielinski, S. Vervoort, H.-W. Mindt, M. Megahed, Influence of Powder Bed Characteristics on Material Quality, Additive Manufacturing. 162 (2017) 192–198.

[16]   M. Bayat, A. Thanki, S. Mohanty, A. Witvrouw, S. Yang, J. Thorborg, N.S. Tiedje, J.H. Hattel, Keyhole-induced porosities in Laser-based Powder Bed Fusion (L-PBF) of Ti6Al4V: High-fidelity modelling and experimental validation, Additive Manufacturing. 30 (2019) 100835. https://doi.org/10.1016/j.addma.2019.100835.

[17]   Y.S. Lee, W. Zhang, Modeling of heat transfer, fluid flow and solidification microstructure of nickel-base superalloy fabricated by laser powder bed fusion, Additive Manufacturing. 12 (2016) 178–188.

[18]   P.S. Cook, A.B. Murphy, Simulation of melt pool behaviour during additive manufacturing: Underlying physics and progress, Additive Manufacturing. 31 (2020). https://doi.org/10.1016/j.addma.2019.100909.

[19]   S.A. Khairallah, A.A. Martin, J.R.I. Lee, G. Guss, N.P. Calta, J.A. Hammons, M.H. Nielsen, K. Chaput, E. Schwalbach, M.N. Shah, M.G. Chapman, T.M. Willey, A.M. Rubenchik, A.T. Anderson, Y.M. Wang, M.J. Matthews, W.E. King, Controlling interdependent meso-nanosecond dynamics and defect generation in metal 3D printing, Science. 368 (2020) 660–665.

[20]   A. v. Gusarov, I. Yadroitsev, P. Bertrand, I. Smurov, Model of radiation and heat transfer in laser-powder interaction zone at selective laser melting, Journal of Heat Transfer. 131 (2009) 1–10. https://doi.org/10.1115/1.3109245.

[21]   T.R. Allen, W. Huang, J.R. Tanner, W. Tan, J.M. Fraser, B.J. Simonds, Energy-Coupling Mechanisms Revealed through Simultaneous Keyhole Depth and Absorptance Measurements during Laser-Metal Processing, Physical Review Applied. 13 (2020). https://doi.org/10.1103/PhysRevApplied.13.064070.

[22]   C. Panwisawas, Y. Sovani, M.J. Anderson, R. Turner, N.M. Palumbo, B.C. Saunders, I. Choquet, J.W. Brooks, H.C. Basoalto, A Multi-Scale Multi-Physics Approach to Modelling of Additive Manufacturing in Nickel-Based Superalloys, Superalloys, John Wiley & Sons, Inc., 2016.

[23]   C. Panwisawas, B. Perumal, R.M. Ward, N. Turner, R.P. Turner, J.W. Brooks, H.C. Basoalto, Keyhole formation and thermal fluid flow-induced porosity during laser fusion welding in titanium alloys: Experimental and modelling, Acta Materialia. 126 (2017) 251–263.

[24]   A. Bauereiss, T. Scharowsky, C. Koerner, Defect generation and propagation mechanism during additive manufacturing by selective beam melting, Journal of Materials Processing Technology. 214 (2014) 2522–2528.

[25]   M. Markl, C. Koerner, Multiscale Modeling of Powder Bed-Based Additive Manufacturing, Annual Reviews. 46 (2016) 93–123.

[26]   A. Klassen, V.E. Forster, V. Juechter, C. Koerner, Numerical simulation of multi-component evaporation during selective electron beam melting of TiAl, Journal of Materials Processing Technology. 247 (2017) 280–288.

[27]   A. Rai, Markl. M., C. Koerner, A coupled Cellular Automaton-Lattice Boltzmann model for grain structure simulation during additive manufacturing, Computational Materials Science. 124 (2016) 37–48.

[28]   Y.A. Mayi, M. Dal, P. Peyre, M. Bellet, C. Metton, C. Moriconi, R. Fabbro, Laser-induced plume investigated by finite element modelling and scaling of particle entrainment in laser powder bed fusion, Journal of Physics D: Applied Physics. 53 (2019) 275–306.

[29]   X. Li, C. Zhao, T. Sun, W. Tan, Revealing transient powder-gas interaction in laser powder bed fusion process through multi-physics modeling and high-speed synchrotron x-ray imaging, Additive Manufacturing. 35 (2020).

[30]   H. Chen, W. Yan, Spattering and denudation in laser powder bed fusion process: Multiphase flow modelling, Acta Materialia. 196 (2020) 154–167.

[31]   S. Jana, O. Kaettlitz, F. Hediger, J. Jakumeit, J. Aguilar, Predictions of misruns using three-phase coupled mold-filling and solidification simulations in low pressure turbine (LPT) blades, in: MCWASP XIII: International Conferene an Modelling of Casting, Welding and Advanced Solidification Processes, 2012.

[32]   I. Demirdzic, S. Muzaferija, Numerical method for coupled fluid flow, heat transfer and stress analysis using unstructured moving meshes with cells of arbitrary topology, Computer Methods in Applied Mechanics and Engineering. 125 (1995) 235–255. https://doi.org/10.1016/0045-7825(95)00800-G.

[33]   A. Teskeredžić, I. Demirdžić, S. Muzaferija, Numerical method for heat transfer, fluid flow and stress analysis in phase-change problems, Numerical Heat Transfer, Part B: Fundamentals. 42 (2002) 437–459.

[34]   J.U. Brackbill, D.B. Kothe, C. Zemach, A continuum method for modelling surface tension, Journal of Computational Physics. 100 (1992) 335–354.

[35]   A. Klassen, T. Scharowsky, C. Koerner, Evaporation model for beam based additive manufacturing using free surface lattice Boltzmann methods, Journal of Physics D-Applied Physics. 47 (2014). http://doi.org/10.1088/0022-3727/47/27/275303.

[36]   C.J. Knight, Theoretical Modeling of Rapid Surface Vaporization with Back Pressure, AIAA Journal. 17 (1979) 519–523. https://doi.org/10.2514/3.61164.

[37]   S.I. ANISIMOV, Vaporization of Metal Absorbing Laser Radiation, 27 (1996) 14–15. https://doi.org/10.1142/9789814317344_0002.

[38]   H. Shen, Influence of Gas Flow Speed on Laser Plume Attenuation and Powder Bed Particle Pickup in Laser Powder Bed Fusion, Jom. 3 (2020) 1039–1051.

[39]   J. Yin, D. Wang, L. Yang, H. Wei, P. Dong, L. Ke, G. Wang, H. Zhu, X. Zeng, Correlation between forming quality and spatter dynamics in laser powder bed fusion, Additive Manufacturing. 31 (2020) 100958. https://doi.org/10.1016/j.addma.2019.100958.

[40]   A.B. Liu, D. Mather, R.D. Reitz, Modeling the effects of drop drag and breakup on fuel sprays, SAE Technical Papers. (1993). https://doi.org/10.4271/930072.

[41]   R. Clift, Drops and Particles, 1978.

[42]   A. Haider, O. Levenspiel, Drag coefficient and terminal velocity of spherical and nonspherical particles, Powder Technology. 58 (1989) 63–70. https://doi.org/10.1016/0032-5910(89)80008-7.

[43]   D.A. Lote, Comparison of Models for Drag and Non-Drag Forces for Gas-Liquid Two-Phase Bubbly Flow, Multiphase Science and Technology. 1 (2018) 31–76.

[44]   Q. Qu, Numerical Study of Transient Deformation and Drag Characteristics of a Decelerating Droplet, AIAA Journal. 8 (2015) 1–16.

[45]   CFD program Simcenter STAR-CCM+ documentation, (2020).

[46]   S. Deb, D.K. Tafti, A novel two-grid formulation for fluid–particle systems using the discrete element method, Powder Technology. 246 (2013) 601–616.

[47]   L. Wang, J. Ouyang, C. Jiang, Direct calculation of voidage in the fine-grid CFD–DEM simulation of fluidized beds with large particles, Particuology. 40 (2018) 23–33.

[48]   J. Bouillard, R. Lyczkowski, D. Gidaspow, Porosity Distributions in a Fluidized Bed with an Immersed Obstacle, AIChE J. 35 (1989) 908–922.

[49]   C.Y. Wen, Y.H. Yu, Mechanics of fluidization, Chemical Engineering Progress Symposium Series. 62 (1966) 100–111.

[50]   S. Ergun, Fluid flow through packed columns, Chemical Engineering Progress. 48 (1952) 9–94.

[51]   C. Springer, Simulation of Air Entrainment in High Pressure Die Casting Applications, 2016.

[52]   K.C. Mills, Recommended values of thermophysical properties for selected commercial alloys, Cambridge, England, 2002.

[53]   Y. Cressault, A.B. Murphy, P. Teulet, A. Gleizes, M. Schnick, Thermal plasma properties for Ar–Cu, Ar–Fe and Ar–Al mixtures used in welding plasmas processes: II. Transport coefficients at atmospheric pressure, Journal of Physics D-Applied Physics. 46 (2013).